Supporting Information

Yang et al. 10.1073/pnas.1705921114

SI Text

Traction-Based Mechanical Inference.

Force balance in the vertex model. Force balance at each vertex requires

$$\boldsymbol{t}_a = \boldsymbol{F}_a, \qquad \textbf{[S1]}$$

where $\boldsymbol{t}_a$ is the traction force vertex a exerts on the substrate, which is balanced by the interaction force $\boldsymbol{F}_a = -\nabla_a E$. We consider for concreteness four adjacent vertices a, b, c, d and corresponding cells i, j, k, as shown in Fig. S1*A*. Using the additivity of the shape energy, we write

$$\boldsymbol{F}_a = -\boldsymbol{\nabla}_a E = -\left(\frac{\partial E_i}{\partial \boldsymbol{r}_a} + \frac{\partial E_j}{\partial \boldsymbol{r}_a} + \frac{\partial E_k}{\partial \boldsymbol{r}_a}\right). \qquad \textbf{[S2]}$$

The right-hand side of Eq. **S2** can be decomposed in terms of tensions and pressure jumps along and perpendicular to the cell edges, as illustrated in Fig. S1*A*, by writing

$$\frac{\partial E_i}{\partial \boldsymbol{r}_a} = -\Pi_i \frac{\partial A_i}{\partial \boldsymbol{r}_a} + T_i \frac{\partial P_i}{\partial \boldsymbol{r}_a}, \qquad \textbf{[S3]}$$

where T_i and Π_i are the cortical tension and hydrostatic pressure for cell i, respectively, defined as (23)

$$T_i \equiv \frac{\partial E_i}{\partial P_i}, \qquad \Pi_i \equiv -\frac{\partial E_i}{\partial A_i}. \qquad \textbf{[S4]}$$

The geometric factors in Eq. **S3** can be written as

$$\frac{\partial A_i}{\partial \boldsymbol{r}_a} = (\hat{\boldsymbol{n}}_{ik} l_{ac} + \hat{\boldsymbol{n}}_{ij} l_{ab})/2, \qquad \frac{\partial P_i}{\partial \boldsymbol{r}_a} = -(\hat{\boldsymbol{l}}_{ab} + \hat{\boldsymbol{l}}_{ac}), \qquad \textbf{[S5]}$$

where $\hat{\boldsymbol{n}}_{ik}$ is the unit vector perpendicular to edge ac pointing from cell i to cell k, l_{ac} is the length of edge ac, and $\hat{\boldsymbol{l}}_{ac}$ is the unit vector along edge ac pointing from vertex a to vertex c. Combining Eqs. **S1**–**S5**, we obtain

$$\begin{aligned}\boldsymbol{t}_a = {} & T_{ab}\hat{\boldsymbol{l}}_{ab} + T_{ac}\hat{\boldsymbol{l}}_{ac} + T_{ad}\hat{\boldsymbol{l}}_{ad} \\ & + \frac{1}{2}\Pi_{ji}\hat{\boldsymbol{n}}_{ji} l_{ab} + \frac{1}{2}\Pi_{jk}\hat{\boldsymbol{n}}_{jk} l_{ad} + \frac{1}{2}\Pi_{ki}\hat{\boldsymbol{n}}_{ki} l_{ac},\end{aligned} \qquad \textbf{[S6]}$$

where

$$T_{ab} = T_i + T_j \quad T_{ac} = T_i + T_k \quad T_{ad} = T_j + T_k \qquad \textbf{[S7]}$$

$$\Pi_{ji} = \Pi_j - \Pi_i \quad \Pi_{jk} = \Pi_j - \Pi_k \quad \Pi_{ki} = \Pi_k - \Pi_i \qquad \textbf{[S8]}$$

are edge tensions and pressure jumps along and across cell edges, respectively. Eqs. **S6**–**S8** form the basis for the traction-based mechanical inference and can be written in a general form as

$$\boldsymbol{F}_a(\{\Pi_i\}, \{T_i\}) = \boldsymbol{t}_a. \qquad \textbf{[S9]}$$

Operationally, we write the force balance equation in a matrix form

$$\boldsymbol{M} \cdot \boldsymbol{\phi} = \boldsymbol{t}, \qquad \textbf{[S10]}$$

where $\boldsymbol{M}$ is a $4N \times 2N$ structural matrix incorporating the orientation and length of the edge vectors, $\boldsymbol{\phi}$ is a $2N \times 1$ column vector whose elements are the cortical tensions and pressures, and $\boldsymbol{t}$ is the $4N \times 1$ column vector of the traction forces at each vertex. The tensions and pressures are obtained by inverting the structural matrix

$$\boldsymbol{\phi} = \boldsymbol{M}^{-1} \cdot \boldsymbol{t}, \qquad \textbf{[S11]}$$

which is equivalent to a least-squares minimization of

$$Tr[(\boldsymbol{M} \cdot \boldsymbol{\phi} - \boldsymbol{t})^T \cdot (\boldsymbol{M} \cdot \boldsymbol{\phi} - \boldsymbol{t})]. \qquad \textbf{[S12]}$$

In practice, this is done with the Moore–Penrose pseudoinverse algorithm implemented using Matlab (25, 45). The pressures are determined up to a global scale since the force balance equations depend only on the pressure differences (Eq. **8**). We set the global scale by requiring the average cellular pressure to be zero, consistent with the simulation where the average area $\bar{A}$ of the cell is equal to the preferred area A_0. For systems with a free boundary condition, as in many experimental setups, the average pressure is determined by the hydrostatic pressure of the fluid surrounding the tissue.

Force balance on the coarse-grained grid. In real tissues, the traction force acts not only at cell vertices, but also at focal adhesions and throughout the basal area of a cell, and can be measured using TFM on a coarse-grained grid. Therefore, we generalize the traction-based mechanical inference by coarse graining the tissue on a Cartesian grid and impose force balance on each grid element (Fig. S1*B*)

$$\boldsymbol{F}_{grid}(\{\Pi_i\}, \{T_i\}) = \boldsymbol{t}_{grid}, \qquad \textbf{[S13]}$$

where $\boldsymbol{F}_{grid}$ is the interaction force on each grid element as calculated from tensions and pressures as shown in Fig. S1*B*, and $\boldsymbol{t}_{grid}$ is the traction force the grid element exerts on the substrate. A grid element is a closed region of the tissue. In a Cartesian grid, it is a square element as highlighted in Fig. S1*B*. The interaction force acts on the grid element through the boundary and is generally expressed as a surface integral, or a line integral in 2D, as

$$\boldsymbol{F}_{grid} = \int_{\partial S} [T_{ab}\hat{\boldsymbol{n}}_{ab}\delta(l - l_s) + \Pi_i \hat{\boldsymbol{n}}_s]\, dl, \qquad \textbf{[S14]}$$

where tension is a point force concentrated at the intersection l_s between the cell edge and the grid element boundary, while pressure induces a normal force in the normal direction $\hat{\boldsymbol{n}}_s$ of the boundary. Note that the pressure varies as the boundary crosses different cells.

Explicit procedure for extracting stress from experimental data. Images of cell interfaces are first segmented using tools such as the watershed algorithm. The segmented cell images are superimposed with the grid system of the TFM as in Fig. S1*B*. This identifies l_s, $\hat{n}_{ab}$, and $\hat{n}_s$ as defined in Eq. **S14**. The traction force the grid element exerts on the substrate t_{grid} can be measured using TFM. Inserting Eqs. **S14** and **S7** into Eq. **S13** yields a matrix equation where the only unknowns are the tensions T_i and the pressures Π_i. Using the Moore–Penrose pseudoinverse algorithm, this equation, together with proper boundary conditions, can be inverted to generate estimations for all tensions and pressures, which can be used to construct the local stress tensor using Eq. **3a** in the main text.

To test the coarse-grained mechanical inference, we generate cell network configurations using the SPV model. The traction force of the grid element is calculated as the sum of tensions (normal forces) on the vertices (cell edges) within the grid element. It is numerically verified that the traction force is exactly balanced by the interaction force for each grid element. We have tested the coarse-grained mechanical inference in our numerical simulation with a grid element size of the order of a single cell size. The inferred stress agrees perfectly with the accurate value obtained from the cell shape, using the energy functional of the tissue (Fig. 2 in the main text).

This coarse-grained mechanical inference requires knowledge of cell shapes as well as traction forces. The cell shape allows one to express the interaction force in terms of tension and pressure and resolves the stress down to a single-cell level. The resolution of the coarse graining can be adjusted to adapt to the resolution of the TFM, where a higher TFM resolution will yield a

more accurate result for the inferred tensions and pressures by overconstraining the system, and make the pseudoinverse better conditioned. Clearly, the extracted stresses will therefore be better constrained as the TFM resolution increases.

The traction-based mechanical inference does not require knowledge of the energy functional or the material property of the tissue and is based on the assumption of force balance and the decomposition of interaction forces into junctional tensions and cell pressures. We expect our method to have general applicability to epithelial tissues where cell shape and traction forces can be measured simultaneously.

Tissue Stress. From cellular tensions and pressures one can also evaluate the mean interaction stress for the whole tissue, given by

$$\sigma^{int}_{\alpha\beta} = -\Pi_T \delta_{\alpha\beta} + \frac{1}{A_T}\sum_{ab} T^{\alpha}_{ab} l^{\beta}_{ab}, \qquad \textbf{[S15]}$$

where the summation is over all edges, A_T is the area of the tissue, and the pressure conjugated to the tissue area A_T is given by

$$\Pi_T = \sum_i \Pi_i \frac{A_i}{A_T}. \qquad \textbf{[S16]}$$

Combining Eq. **3a** in the main text with Eqs. **S15** and **S16**, we show that the interaction tissue stress is related to the cellular stress as

$$\sigma^{int}_{\alpha\beta} = \frac{1}{A_T}\sum_i A_i \sigma^{(i)int}_{\alpha\beta}. \qquad \textbf{[S17]}$$

Next we show that for the energy functional given by Eq. **1** of the main text, the tissue interaction normal stress can be expressed in terms of cell areas and perimeters. We first focus on the interaction normal stress of cell i defined as

$$\sigma^{(i)int}_{n} = \frac{1}{2}\left(\sigma^{(i)int}_{xx} + \sigma^{(i)int}_{yy}\right). \qquad \textbf{[S18]}$$

Using Eq. **3a** in the main text, we rewrite Eq. **S18** as

$$\sigma^{(i)int}_{n} = -\Pi_i + \frac{1}{4A_i}\sum_{j\in n.o.i}[(T_i + T_j)l_{ij}], \qquad \textbf{[S19]}$$

where we used the relation in Eq. **S7** and the summation is over the neighbors of cell i. l_{ij} is the length of the edge shared by cell i and cell j. Using the energy functional (Eq. **1** in the main text) and the definitions for tension and pressure (Eq. **S4**), we have

$$\sigma^{(i)int}_{n} = 2K_A(A_i - A_0) + \frac{K_P}{2A_i}\sum_{j\in n.o.i}[(P_i - P_0)l_{ij} + (P_j - P_0)l_{ij}]. \qquad \textbf{[S20]}$$

Substituting Eq. **S20** into Eq. **S17**, we obtain the interaction normal stress for the tissue in terms of cell areas and perimeters

$$\sigma^{int}_{n} = \frac{1}{A_T}\sum_i [2K_A A_i(A_i - A_0) + K_P P_i(P_i - P_0)], \qquad \textbf{[S21]}$$

where we used the identity

$$\sum_{j\in n.o.i} l_{ij} = P_i \qquad \textbf{[S22a]}$$

$$\sum_i \sum_{j\in n.o.i}(P_j - P_0)l_{ij} = \sum_i (P_i - P_0)P_i. \qquad \textbf{[S22b]}$$

Eq. **S21** expresses the interaction tissue stress in terms of cell shape parameters, providing a prescription for extracting mechanical information directly from cell images. We plot the mean normal interaction stress (Eq. **S21**) and the mean normal swim stress (Eq. **6** in the main text) as a function of v_0 and P_0 in Fig. S2. Note that the interaction stress is contractile and the swim stress is extensile. The latter vanishes in the solid state and dominates deep in the liquid state, resulting in a change of sign of the total normal stress as shown in Fig. 3 in the main text.

Effect of A_0 on cell dynamics. For a system with periodic boundary conditions and fixed system size and cell number, the parameter A_0 plays no essential role in the cell dynamics. It renormalizes the pressure of the system only by a constant, but does not affect cell shapes, forces on vertices, or the anisotropic part of the stress tensor. To see this, we rewrite the energy of the system, using the average cell area $\bar{A}$. Up to a constant offset, the total energy reads

$$E = \sum_{i=1}^{N}\left[K_A(A_i - \bar{A})^2 + K_P(P_i - P_0)^2\right] + \frac{1}{N}K_A A_T^2 - 2K_A A_T A_0. \qquad \textbf{[S23]}$$

Note that the parameter A_0 appears only in the last term of Eq. **S23**, which merely offsets the pressure of the system by $2K_A A_0$. Thus, all forces $\boldsymbol{F}_i$ and shear stresses are independent of A_0. The liquid–solid phase transition is unaffected by A_0 as shown in Fig. S3.

Effect of Voronoi constraint on the tissue stress. The SPV model can be mapped to an active vertex model (AVM) with effective constraints imposed by the Voronoi tessellation on the vertex positions. In a vertex model free of Voronoi constraint, the interaction stress tensor $\sigma^{int}_{\alpha\beta}$ defined by Eq. **6** in the main text represents precisely the stress acting on the periodic boundary. This is not, however, the case for the SPV model, because the creation of cell shapes using a Voronoi tessellation adds constraints to a vertex model. In this section, we show that the results presented in this paper are robust against the Voronoi constraint.

The normal stress defined in Eq. **10** in the main text is unaffected by the Voronoi constraint, but the shear stress does not correspond to the shear stress at the boundary of the system. This is because an affine shear deformation of all cell positions does not induce an affine shear transformation of all vertex positions. Indeed, the $2N$ vertices would in total provide $4N$ degrees of freedom, but the Voronoi tessellation reduces this to the $2N$ degrees of freedom of the N cell positions.

In the SPV model, the stress experienced by the boundary can be computed by quantifying the total energy change induced by a deformation of the periodic box described by the strain tensor $G_{\alpha\beta}$ while affinely displacing all cell positions and respecting the Voronoi tessellation,

$$\tilde{\sigma}^{int}_{\alpha\beta} = \frac{1}{A_T}\frac{dE}{dG_{\alpha\beta}}, \qquad \textbf{[S24]}$$

where the tilde is used to denote the stress at the boundary under Voronoi constraint. The shear component of this tensor is different from that of the stress $\sigma^{int}_{\alpha\beta}$ defined in Eq. **6** in the main text.

To numerically study how different $\tilde{\sigma}^{int}_{\alpha\beta}$ and $\sigma^{int}_{\alpha\beta}$ typically are, we impose a sufficiently small strain on the cell positions and calculate the tissue energy difference before and after the imposed strain. To incorporate the Voronoi constraint, the cell network is constructed based on the cell positions before and after the imposed strain according to the Voronoi tessellation. An expansion along the x and the y axis is implemented to compute the normal components of the stress $\tilde{\sigma}^{int}_{xx}$ and $\tilde{\sigma}^{int}_{yy}$, using

$$\tilde{r}^i_x = r^i_x(1+\epsilon), \quad \tilde{r}^i_y = r^i_y(1+\epsilon), \qquad \textbf{[S25]}$$

respectively. Here, $\boldsymbol{r}$ is the cell position and $\epsilon \ll 1$ is the imposed strain. Similarly, simple shear deformations along x and y axes are implemented to compute the off-diagonal components of the stresses $\tilde{\sigma}^{int}_{xy}$ and $\tilde{\sigma}^{int}_{yx}$, using the transformations

$$\tilde{r}^i_x = r^i_x + \epsilon r^i_y, \quad \tilde{r}^i_y = r^i_y + \epsilon r^i_x, \qquad \textbf{[S26]}$$

respectively.

We present the results of the stress at the boundary under Voronoi constraint in Fig. S4. Compared with the results in the main text, the effect of the Voronoi tessellation does not affect the behavior of the normal and the shear stress as presented in the main text. This suggests that for practical purposes, one can apply the definitions of stress of the vertex model to approximate the stress in the SPV model. The insensitivity of the behavior of the stress to the geometrical constraint also implies general applicability of the SPV model in describing the mechanics of confluent epithelial tissue in experiment.

Autocorrelation of traction forces. The slowing down of the autocorrelation of the shear stress implies a similar behavior for the autocorrelation of traction forces due to the force balance condition $t_\alpha = \partial_\beta \sigma^{int}_{\alpha\beta}$. We have shown this explicitly by evaluating the autocorrelation function of the vertex tractions averaged over a small patch of tissue as a function of v_0 and P_0, as shown in Fig. S5. In contrast to the shear stress, we cannot average the traction over the entire system, as due to force balance the net traction force is zero. Instead we compute the two-time correlation function of the traction forces averaged over a circular patch of tissue of radius R. Such a mean local traction is calculated in two reference frames: the Eulerian frame where the circular patch of radius $R = 0.1L$ is fixed in space (Fig. S5*A*) and the Lagrangian reference frame where cells initially within the patch are tracked in time (Fig. S5*D*). To reduce the finite-size fluctuations, we compute the autocorrelation using seven patches at different positions and average over the patches. Experimental traction forces are usually measured in a Eulerian reference frame by TFM. Such measurements could, however, be transformed to a Lagrangian reference frame if cell tracking data are available.

Fig. S5 *B* and *E* shows the autocorrelation of the traction, $C_{tt}(\tau) = \langle t_x(t_0) t_x(t_0+\tau)\rangle_{t_0}$, with t_x the x component of the average traction in the Eulerian and Lagrangian frames, respectively. When calculated in the Lagrangian frame, the correlations show the same dramatic slowdown when the solid is approached from the liquid side as found in the autocorrelation of the mean shear stress. In the Eulerian frame, however, a second timescale associated with cells moving in and out of the fixed patch masks the slowing down of the relaxation at long times. The same behavior is obtained when calculating correlations of shear stress averaged over a local patch instead of over the entire system. The slowing down of the relaxation is quantified in Fig. S5 *C* and *F*, which shows heat maps of the correlation time τ_m defined as $C_{tt}(\tau_m)/C_{tt}(0) = 0.02$ in the Eulerian and Lagrangian frames, respectively. The correlation time increases as the system transits from the fluid state to the solid state in both reference frames and diverges deep in the solid state. The behavior is less clear in the Eulerian reference frame, where cell transition across the patch introduces a new timescale that masks the divergence. In summary, this confirms that the divergence of traction and shear relaxation can in principle be seen in TFM data, especially if combined with cell tracking so that correlations can be computed in a Lagrangian frame. Our results suggest a unique way of analyzing TFM data to provide rheological information about the tissue.

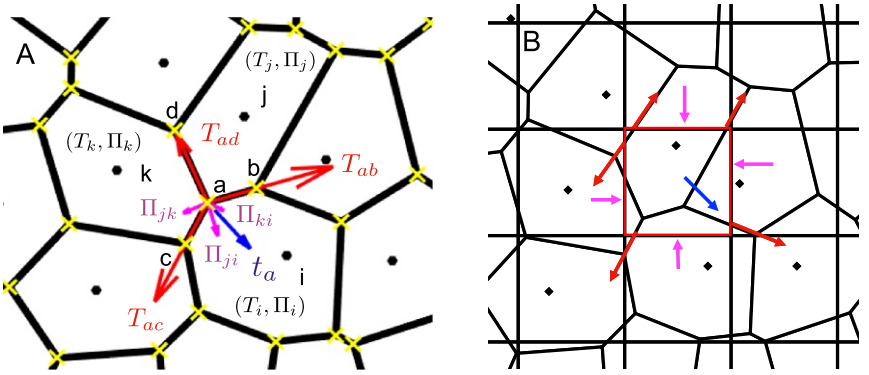

Fig. S1. (*A*) Schematic of force balance at vertex *a* joining the neighboring cells *i*, *j*, *k*, with tangential forces from edge tensions (red) and normal forces from pressure differences (magenta). The edge tensions at vertex *a* are determined by the sum of the cortical tensions (T_i, T_j, T_k) of the neighboring cells (Eq. **S7**). The normal forces are determined by the difference of the pressures (Π_i, Π_j, Π_k) of the neighboring cells (Eq. **S8**). $\boldsymbol{t}_a$ is the traction force vertex *a* exerts on the substrate. (*B*) Schematic of force balance at the coarse-grained grid. The interaction force on the grid element (red arrow for tension and magenta arrow for pressure-induced normal force) balances the traction force (blue arrow) the grid element exerts on the substrate.

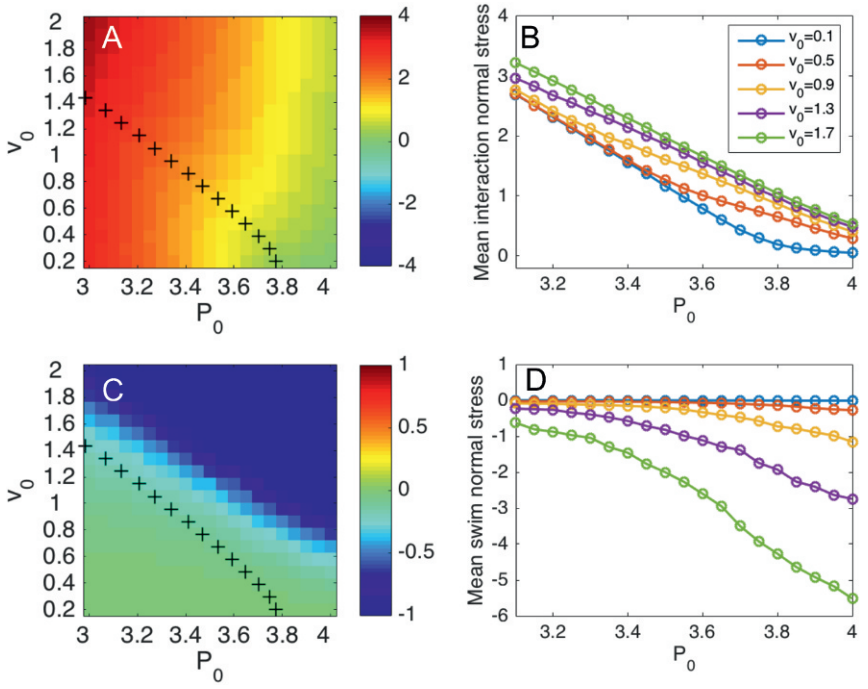

Fig. S2. (*A* and *C*) Heat map of the mean interaction (swim) normal stress of the tissue in the (v_0, P_0) plane. The black crosses outline the solid–liquid phase boundary determined by $q = 3.813$. Red indicates contractile stress and blue extensile stress. (*B* and *D*) Mean interaction (swim) normal stress as a function of P_0 for various v_0 (400 cells for $T = 1,000$ and $D_r = 0.1$).

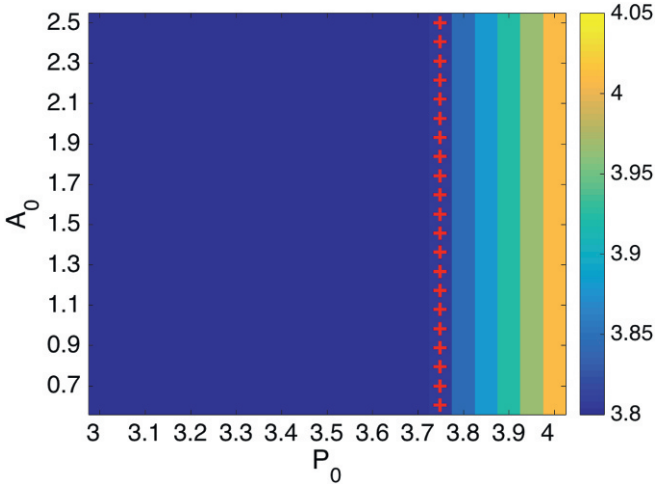

Fig. S3. Phase diagram in the (A_0, P_0) plane at $v_0 = 0.2$. The red crosses outline the solid–liquid phase boundary determined by $q = 3.813$. Note that A_0 does not affect the liquid–solid phase transition. The simulation is performed using the SPV model for a duration of $T = 1,000$ with 400 cells at $D_r = 1.0$ with periodic boundary condition.

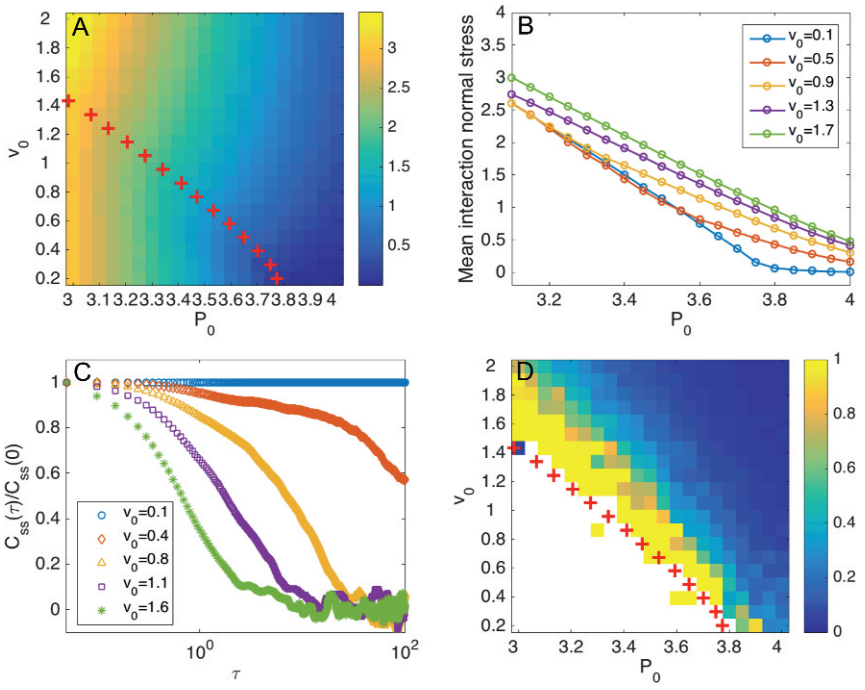

Fig. S4. Behavior of normal and shear tissue stress with Voronoi constraint from the energy derivative with respect to imposed strain (Eq. **S24**). (*A*) Heat map of the mean interaction normal stress as a function of v_0 and P_0. The red crosses outline the solid–liquid phase boundary determined by $q = 3.813$. (*B*) Mean interaction normal stress as a function of P_0 at various v_0. (*C*) Time autocorrelation of the mean interaction shear stress for various v_0 at $P_0 = 3.45$. (*D*) Heat map of the effective viscosity (Eq. **13** in the main text). The simulation is performed with 100 cells and a duration of $T = 1,000$ with periodic boundary condition.

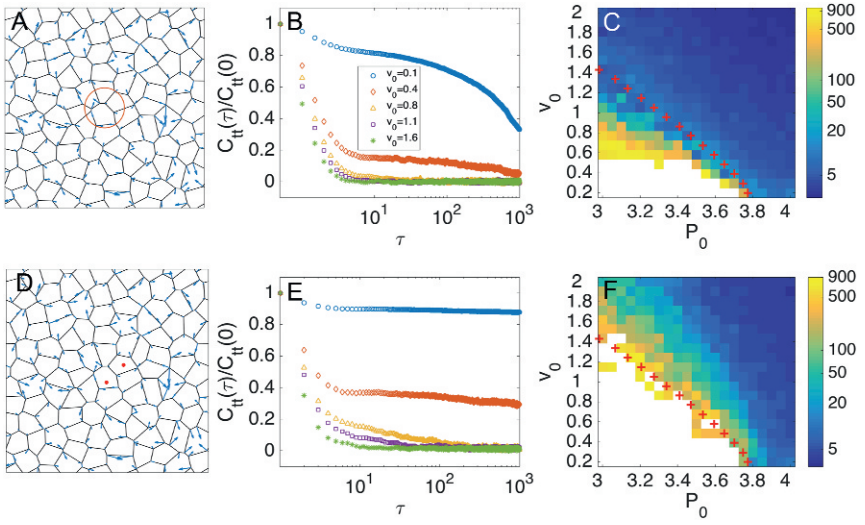

Fig. S5. The time autocorrelation of traction force slows down as the tissue transits from fluid state to solid state. (*A–F*) The autocorrelation evaluated in the Eulerian (*A–C*) and Lagrangian (*D–F*) reference frames. (*A*) Vertex tractions are averaged within a circle of radius $R = 0.1L$ fixed in space, where L is the length of the simulation box. (*D*) Average tractions at vertices of cells initially located within a circle of radius $R = 0.1L$ and then tracked in time (the corresponding cells are labeled in red). (*B* and *E*) Normalized autocorrelation of traction force at $P_0 = 3.45$ in the Eulerian (*B*) and Lagrangian (*E*) frames. (*C* and *F*) Heat maps of the correlation time τ_m in the Eulerian (*C*) and Lagrangian (*F*) frames. The white region corresponds to correlation time beyond the duration of the simulation. The simulation is performed over a total time $T = 10,000$ for 100 cells with $D_r = 1.0$ and periodic boundary condition.